

RESEARCH ARTICLE | JULY 06 2005

Electron-beam-induced deformations of SiO₂ nanostructures

A. J. Storm; J. H. Chen; X. S. Ling; H. W. Zandbergen; C. Dekker



Journal of Applied Physics 98, 014307 (2005)

<https://doi.org/10.1063/1.1947391>



CrossMark

AIP Advances

Why Publish With Us?



25 DAYS
average time
to 1st decision



740+ DOWNLOADS
average per article



INCLUSIVE
scope

[Learn More](#)

Electron-beam-induced deformations of SiO₂ nanostructures

A. J. Storm^{a)}

Kavli Institute of Nanoscience, Delft University of Technology, Lorentzweg 1, 2628 CJ Delft, The Netherlands

J. H. Chen

Kavli Institute of Nanoscience, Delft University of Technology, Lorentzweg 1, 2628 CJ Delft, The Netherlands and Netherlands Institute for Metals Research, 2628 AL Delft, The Netherlands

X. S. Ling,^{b)} H. W. Zandbergen, and C. Dekker

Kavli Institute of Nanoscience, Delft University of Technology, Lorentzweg 1, 2628 CJ Delft, The Netherlands

(Received 13 September 2004; accepted 12 May 2005; published online 6 July 2005)

The imaging beam of a transmission electron microscope can be used to fine tune critical dimensions in silicon oxide nanostructures. This technique is particularly useful for the fabrication of nanopores with single-nanometer precision, down to 2 nm. We report a detailed study on the effect of electron-beam irradiation on apertures with various geometries. We show that, on the same wafer, pores that are smaller than a certain critical size shrink and that larger ones expand. Our results are in agreement with the hypothesis that surface-tension effects drive the modifications. Additionally, we have determined the chemical composition in the pore region before and after modifications and found no significant changes. This result proves that contamination growth is not the underlying mechanism of pore closure. © 2005 American Institute of Physics.

[DOI: 10.1063/1.1947391]

I. INTRODUCTION

Fabrication of devices with dimensions on the single-nanometer scale is important for many electrical, biological, and chemical applications. Currently, lithographical techniques including electron-beam lithography are not precise enough to obtain devices with this level of control.¹ Bottom-up approaches, such as scanning probe manipulation of individual atoms or molecules on a surface,^{2–4} can obtain precision at the atomic scale, but they are inherently slow and have only a narrow range of applications in device fabrication. It was recently realized that control over dimensions with nanometer precision can be obtained with suitable feedback during processing of a nanostructure. For example, Morpurgo *et al.*⁵ demonstrated that metallic electrodes with nanometer spacing can be made by electroplating. During the electroplating, the conductance between the two electrodes is measured, which is a measure for the distance. Another example is the ion-beam sculpting technique reported by Li *et al.*:⁶ apertures of about 60 nm could be reduced to 2 nm by ion-beam sputtering while continuously measuring the ion flux through the aperture. This ion flux is proportional to the area of the aperture, and the process can be stopped once the desired area has been obtained. In both these examples feedback is used to gain control over a critical dimension in the nanoscale device during processing.

Inspired by this principle, we report another technique to fabricate nanostructures with single-nanometer precision,⁷ with direct visual feedback. We employ the electron beam of

a transmission electron microscope to controllably shrink apertures in silicon oxide with an initial size of 20–50 nm. The image of the microscope provides real-time feedback during shrinking, and thus both the size and the shape of the aperture are known throughout the process. We can stop the process at the desired dimension by blanking the beam and obtain a high yield of round nanopores with a final diameter well below 10 nm, with an estimated precision of 1 nm.

Currently, there is a strong and growing interest in solid-state nanopores for single-molecule translocation studies.^{6,8–13} Our technique was developed specifically for this purpose. Recently, Li *et al.*⁸ demonstrated that the ion-beam-sculpted nanopores can be used to detect individual double-stranded DNA molecules at the single-molecule level. Quantized current blockades, caused by the passage of individual molecules, are reported and used to analyze the folding behavior of the molecule. It has been speculated⁸ that integration of additional sensors near the nanopore will eventually allow DNA sequencing at the single-molecule level.

In this work, we present a detailed experimental study of deformation processes of silicon oxide nanostructures induced by an electron beam and observed with a transmission electron microscope (TEM). We start with a description of the fabrication process that we use to make the silicon oxide structures. Subsequently, an extensive set of experiments on nanopores with various geometries is reported. In particular, we show the interesting effect that small pores shrink while, under the same conditions, larger pores expand in the electron microscope. An important issue that we address in this work concerns possible changes in the chemical composition of the materials irradiated with the electron beam. First, there is the risk that the electron beam promotes the deposition of

^{a)}Electronic mail: storm@mb.tn.tudelft.nl

^{b)}Permanent address: Department of Physics, Brown University, Providence, Rhode Island 02912.

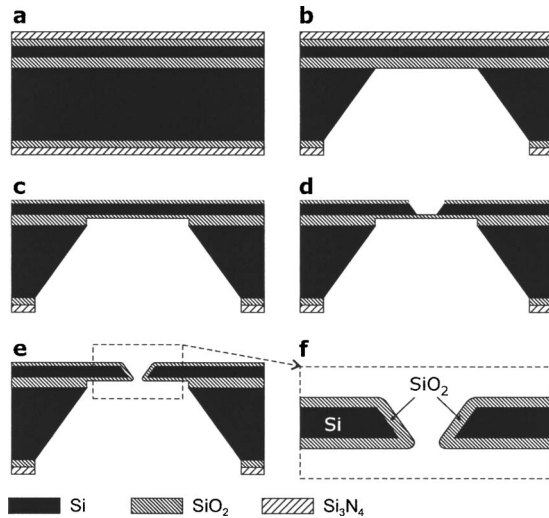


FIG. 1. Cross-sectional view of the silicon device at several stages during fabrication. (a) SOI wafer with protective layers. (b) Freestanding silicon membranes with protective layers. (c) After removal of the protective layers, the bare silicon membranes are thermally oxidized. (d) After a second lithography step, KOH is used to etch small pores in the silicon membrane. (e) The residual SiO₂ is removed from the device to open up the pores in the membrane. Subsequently, a thin silicon oxide layer is grown on the surfaces of the membrane and pore. (f) Enlarged, cross-sectional view of the silicon oxide pore shown in panel (e).

carbon-rich material on the device, which could give rise to another mechanism for pore closure. A second effect concerns potential changes in the composition of the silicon oxide by the high-energy electrons bombarding it. To address these issues, a number of control experiments have been performed. We show that these effects play, at most, only a minor role in the process.

In an earlier work, we argued that the electron beam fluidizes the silicon oxide,⁷ and that the surface tension leads to the observed shape changes. Here, we present a refined model using local Laplace pressures generated at curved, liquid surfaces. We use this formalism to explain and understand the size and shape evolution of our nanopores in more detail.

II. MATERIALS AND METHODS

A. Fabrication of silicon oxide nanostructures

The fabrication of the silicon oxide structures that we modify inside the TEM microscope builds upon the work by Gribov *et al.*¹⁴ The starting material is a silicon-on-insulator wafer (SOITEC, France) with a diameter of 100 mm. The wafer consists of a 525- μm -thick “handle” wafer, with a buried oxide layer of 400 nm and a silicon “device” top layer 340 nm thick. We will further denote the side of the wafer containing the device layer as the front side. Both the handle wafer and the thin device layer are $\langle 100 \rangle$ silicon single crystals and are p doped with a conductivity of 20–30 $\Omega\text{ cm}$. The wafer is covered on both sides with a 100-nm-thick TEOS silicon oxide layer. Subsequently, a 100-nm low-pressure chemical-vapor deposition (LPCVD)-grown Si₃N₄ layer is deposited on both sides [see Fig. 1(a)]. Then we perform electron-beam lithography and subsequent CHF₃/O₂ plasma etching on the backside of the wafer [see Fig. 2(a)] for

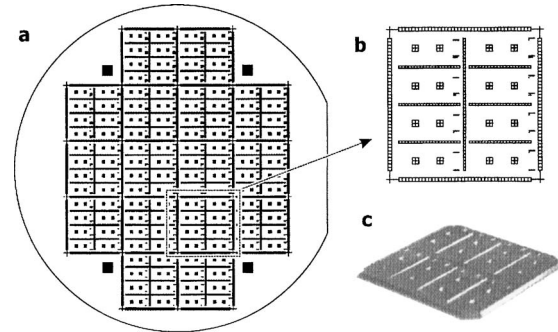


FIG. 2. (a) Pattern for the fabrication of membranes on the 100-mm SOI wafer. Using electron-beam lithography, this pattern is written at the backside of the wafer. After pattern transfer to the silicon nitride layer and silicon oxide layers, a KOH etching is performed. The 770 \times 770- μm^2 squares result in 70 \times 70- μm^2 membranes on the front side. Additionally a set of breaking lines is fabricated that will be used to break the wafer first into smaller chips of 17 \times 17 mm², and finally into 5 \times 9-mm² samples, each containing two membranes. The four large squares aid in visually detecting the end point of the KOH etch through the wafer. Note that the patterns contain large unexposed areas in the interior, to save time in the electron-beam lithography exposure. These unexposed regions will be underetched quickly in the hot KOH bath, and the final result is undistinguishable to fully exposed patterns. (b) Close up of the pattern of a 17 \times 17-mm² section of the wafer. The outer lines result in 480- μm -wide V grooves in the wafer. Additionally seven thinner lines are written for later dicing into devices that fit in the transmission electron microscope. Each of these samples contains a set of markers for identification. (c) Photograph of an actual 17 \times 17-mm² chip, viewed from the backside.

the exposed pattern]. After stripping the residual resist the TEOS oxide is removed in the pattern by a wet buffered-hydrofluoric acid (BHF) etch. Using the remaining silicon nitride as a mask we perform a wet KOH etch (300 g/l, 80 $^{\circ}\text{C}$) to obtain pyramid-shaped holes through the handle wafer. This results in thin membranes composed of the silicon device layer and the additional protection layers [see Fig. 1(b)]. The buried oxide layer can be used as an etch stop, due to the slow etch rate of silicon oxide in the KOH solution. Next to the membranes, V-shaped grooves are etched at this stage to break the wafer in smaller pieces at a later stage. A quick dip in hydrochloric acid is performed directly after removal from the KOH to prevent residues. The top silicon nitride layer is removed with a SF₆/O₂ plasma etch. At this stage the sample contains membranes formed by the silicon device layer, covered at the top with the TEOS silicon oxide layer and at the bottom by the buried oxide layer. To obtain bare, freestanding silicon membranes we remove both oxide layers using BHF. The silicon membranes are then thermally oxidized at 1000 $^{\circ}\text{C}$ to obtain a high-quality 50-nm-thick silicon oxide layer on both sides. In Fig. 1(c) we show a cross section of the device at this stage. These silicon oxide layers act as a masking layer in the second stage of anisotropic KOH etching, where the actual nanopores are formed.

At this stage, the full 100-mm wafer is diced up into smaller samples of 17 \times 17 mm² using the V grooves. This dicing can easily be performed by hand by placing the wafer on the edge of a Perspex plate and gently applying some pressure. Each wafer yields 16 dice of 17 \times 17 mm², and each die contains a total of 16 membranes. In this way, we obtain a total of 256 silicon membranes for each 100-mm wafer.

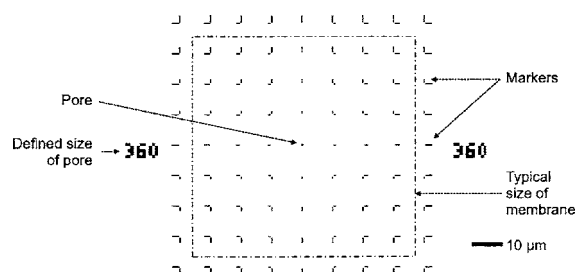


FIG. 3. Typical pattern written on a membrane for fabrication of a single nanopore. In the center is a square of in this case $360 \times 360 \text{ nm}^2$ that will be transferred to the silicon oxide layer. During KOH etching a pyramid-shaped pore will be etched at this position. Around the center square an array of markers is patterned. After KOH etching these markers lead to shallow V grooves in the silicon layer. These markers help to locate the pore in the electron microscope. Additionally the defined size of the center square is written. Each digit consists of $100 \times 100 \text{ nm}^2$ dots and will only etch about 100 nm into the silicon layer of about 300 nm thick.

The second part of the fabrication recipe consists of a second lithography and anisotropic KOH etching step, but at a scale roughly 1000 times smaller. This final fabrication step was performed on $17 \times 17 \text{ mm}^2$ samples. After spinning resist, we pattern the membranes from the front side using electron-beam lithography. On most membranes we used patterns similar to the one shown in Fig. 3. Such patterns were used for the fabrication of a single pore in the membrane, as used in experiments on DNA translocation.^{9,10} Patterns containing more than 100 pores with various shapes and sizes were used for the experiments described in this work. Four membranes on each chip were used as markers to align the exposed patterns with the membranes. After developing, the pattern is transferred to the silicon oxide mask layer by CHF_3/O_2 reactive-ion etching. We now strip the remaining resist in an oxygen plasma. We then etch the sample 2 min in KOH (330 g/l, 60°C) to obtain pyramid-shaped holes through the silicon device layer, as shown in Fig. 1(e). Directly afterwards we rinse the sample in diluted hydrochloric acid and remove the oxide on both sides of the membrane by BHF. Finally, we again thermally oxidize the device to obtain a layer of silicon oxide on all silicon surfaces. As the final result, the surface of the pore and the membrane will be covered with silicon oxide layer, as shown in Figs. 1(e) and 1(f). We studied samples with various thicknesses of the final oxide layer.

B. Electron microscopy

For inspection of the devices at various steps in the fabrication process, we used scanning electron microscopy (SEM). The SEM images shown in this chapter work are obtained with a Hitachi S-900 microscope, operated at an acceleration voltage of 30 kV. This microscope allows tilting of about 50° along one axis.

The deformation of our silicon oxide nanostructures during electron irradiation was studied using TEM. The majority of the experiments were performed using a Philips CM30-UT field-emission microscope operated at an accelerating voltage of 300 kV. The nanopore specimen is mounted on a specially developed holder. The electron microscope allows beam parameters such as diameter and current to be

varied. Typically, we worked with a beam diameter between 100 and 500 nm and an electron dose between 10^4 and 10^7 A m^{-2} .

The Philips CM-30UT microscope is equipped with an energy-dispersive x-ray (EDX) detector. This technique allows measurements on the chemical composition of the specimen, by measuring the spectrum of the x rays generated by the electron scattering.

Additionally, electron-energy-loss spectroscopy (EELS) was performed using a FEI TECNAI200-FEG electron microscope, operated at 200 kV. The obtained spectra can be used to determine the composition of the material. These EELS experiments were performed with the entrance of the spectrometer in the focal plane of the microscope. As a result, all detected electrons are coming from a well-defined part of the specimen.

III. RESULTS

We discuss a number of experiments performed to test our hypothesis that the surface tension of the fluidized silicon oxide drives the morphological changes induced by the TEM electron beam. For these experiments we fabricated silicon membranes with more than 100 pores, in arrays with a pitch of $2 \mu\text{m}$. Slits were fabricated within the same membrane as well. These slits are $1 \mu\text{m}$ long, and the width varies from 20 to about 100 nm. With this approach we have a large number of apertures in the membrane, with various sizes and shapes. The effect of the electron beam can be studied on each structure individually, since we use an electron beam of $1\text{-}\mu\text{m}$ diameter or smaller.

A. Geometry of fabricated structures before modification

Our hypothesis that surface tension drives the observed changes of our nanostructures makes the exact shape of the silicon oxide surface an important experimental parameter. In this section we address this issue based on knowledge of the fabrication process and scanning electron microscopy of our devices.

We first consider the shape of a pore before the last oxidation step. At this stage the pore has a truncated pyramid shape. This geometry is a direct result of the highly anisotropic nature of the wet KOH etch in single-crystal silicon. The surface of the silicon device layer is a (100) crystal plane. The etch rate depends strongly on the crystal direction, and the etch rate in the $\langle 100 \rangle$ direction is at least 100 times faster than in the $\langle 111 \rangle$ direction.¹⁵ This means that the silicon etch will practically stop at the (111) crystal planes. These planes are oriented at an angle of 54.7° with respect to the surface of the membrane. In Fig. 4(a) we show a scanning electron microscope image of a nanopore at this stage. The four sides of the pore are (111) crystal planes. At this stage the silicon edge at the bottom of the pore is almost atomically sharp [see the assumed cross section in Fig. 5(a)]. The next step is to grow a silicon oxide layer by thermally oxidizing the silicon surface. Figure 4(b) shows another nanopore after growth of 50 nm of silicon oxide. This pore has an aperture of about $70 \times 70 \text{ nm}^2$, and is surrounded by sili-

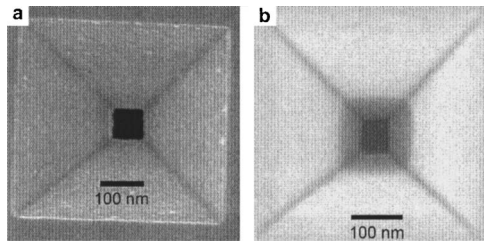


FIG. 4. Scanning electron micrographs of pores in the silicon membrane before and after the final oxidation step. (a) The black square in the middle is an open pore of about 80 nm in the silicon membrane. The anisotropic KOH etching of the single-crystal silicon leads to the inverted pyramid shape of the pore. (b) A different pore after growing a thermal silicon oxide layer of about 50 nm. In this case the pore is about 70 nm wide, and is surrounded by about 40 nm of silicon oxide. Further from the pore the silicon core of the membrane can be seen in light gray. Note that the pore is still square; the oxide layer does not lead to visible rounding of the perimeter of the pore.

con oxide. This silicon oxide is visible as a dark gray region around the black pore in the SEM micrograph. The silicon underneath the oxide can be seen as a light gray region about 40 nm away from the pore. Note that the pore is still square after the oxidation process. We also note that we never observed any changes in size or shape of the silicon oxide pores in the SEM microscope.

The initially sharp edge at the bottom of the pore rounds significantly during the oxidation process. Oxygen gas diffuses through the oxide layer during oxidation and it reacts with the silicon underneath, “pushing” the silicon oxide away. In Fig. 5(b), we sketch the assumed cross section of a pore with a thick oxide layer. In Figs. 5(c) and 5(d), we show SEM micrographs obtained at a tilt angle of about 30° of a bare silicon pore and a pore with a thermal oxide layer of about 80 nm. Clear rounding in the vertical direction is observed for the oxidized pore. Figure 5(e) shows a SEM image of a nanopore that has been cleaved and demonstrates the rounding even more clearly. Based on these images, we estimate that the radius of curvature in the vertical direction is about equal to the thickness of the silicon oxide.

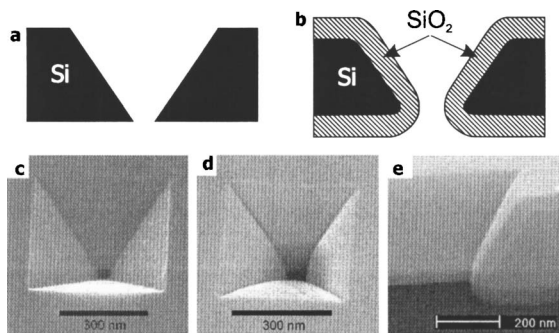


FIG. 5. Rounding of the pore during thermal silicon oxide growth. (a) Schematic, cross-sectional view of a silicon membrane with a pore. Note the sharp angle at the bottom. (b) Expected pore cross section after growth of a silicon oxide layer. (c) SEM micrograph of a pore before oxidation, at a tilt angle of about 30° to reveal the three-dimensional shape. (d) Pore with a thick silicon oxide layer of about 80 nm at a tilt angle of about 30° . (e) Micrograph of a cleaved nanopore to allow imaging of its cross section. A 50-nm oxide layer is visible on the surface of the silicon membrane and pore. Note the clear rounding of the silicon oxide layer around the silicon edge.

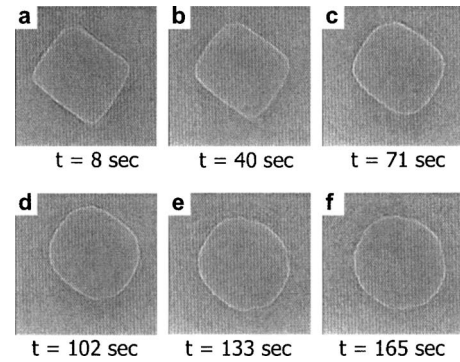


FIG. 6. (a)–(f) Rounding of the perimeter of a $40 \times 45\text{-nm}^2$ pore during the first minutes of TEM imaging.

B. TEM-induced shape changes of rectangular pores

We found that strong irradiation by the electron beam in the TEM deforms the shape of the silicon oxide nanostructures. A minimal electron dose of about 10^4 A m^{-2} is needed to induce changes. The first interesting effect that we observe for all rectangular apertures is that the corners quickly round off. This rounding occurs within minutes after irradiation. Figure 6 shows a sequence of TEM micrographs of a $40 \times 45\text{-nm}$ pore that shows clear rounding during imaging. Apparently, the first changes in the pore occur at the corners, not at the straight segments. This effect will be discussed in Sec. IV.

C. Shrinking and expanding nanopores

We now present a set of experiments to demonstrate the influence of the initial geometry on the nature of deformations of pores, and in particular our main result: pores below a certain size shrink, while larger ones expand. We denote the boundary diameter between these effects as the “critical” diameter. In this section we show this effect explicitly. Two parameters were varied: The initial lateral size of the pore, and the thickness of the oxide grown in the last fabrication step. As discussed in Sec. III A the final oxide thickness is important for the shape of the pore.

First, we show a series of experiments performed on four pores with a final oxide thickness of 50 nm. All pores were located within the same membrane, and imaged with a similar electron beam. We first obtained a high-resolution image with the slow-scan charge-coupled device (CCD) to determine the initial dimensions of each pore. Subsequently we switched to video-rate imaging with a fast-scan CCD sensor to obtain movies of the deforming pores. In Fig. 7 we show three snapshots from each movie, for pores with initial sizes of 40, 55, 80, and 100 nm, respectively. We denote the initial size as the average of the two sides of the rectangular shape. From the micrographs we see that pores of 40- and 55-nm sizes close down and that the 100-nm pore expands. The 80-nm pore shows very little changes other than rounding. This experiment clearly demonstrates the existence of a “critical size”: Smaller pores shrink and larger pores expand. We estimate that for this device, the critical size is $80 \pm 20 \text{ nm}$.

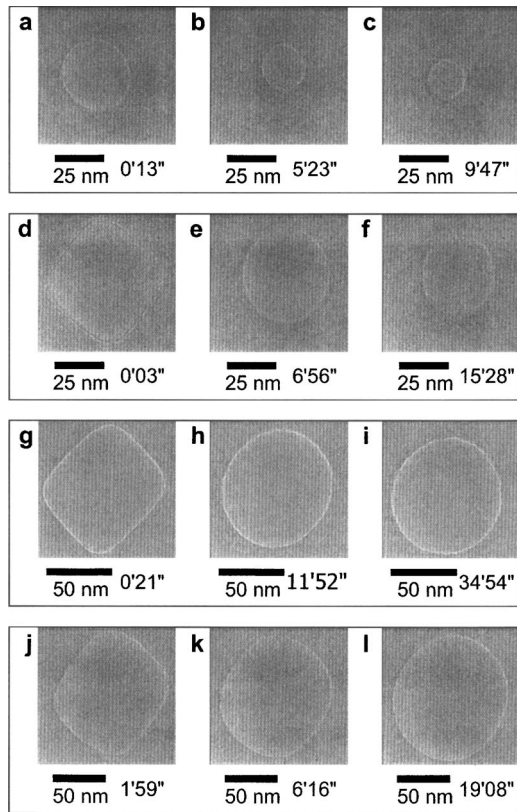


FIG. 7. Nanopore size and shape as a function of irradiation time (denoted at the bottom right below each image). (a)–(c) TEM micrographs of a nanopore with an initial size of about 40 nm. (d)–(f) TEM micrographs of a nanopore with an initial size of about 55 nm. (g)–(i) TEM micrographs of a nanopore with an initial size of about 80 nm. (j)–(l) TEM micrographs of a nanopore with an initial size of about 100 nm.

A second sample was prepared with an array of pores of various sizes, but now with a final oxide thickness of only 20 nm. Here we expect a much sharper apex of the pore, and we show how this affects the pore dynamics. The experiment was performed under similar conditions as the previous one. Figure 8 shows the result for four pores with initial sizes of 15, 30, 35, and 40 nm. We find that the 15-nm pore shrinks, and the 35- and 40-nm ones expand. The size of the 30-nm pore stays quite constant during the experiment. For this device we find a critical size of 25 ± 10 nm, which is significantly smaller than for the thick-oxide sample.

D. Rate of nanopore closure

As shown in Fig. 8, the time scale for typical deformations is on the order of minutes to tens of minutes. Typical rates are on the order of 1 nm/min or slower, depending on the electron dose. Figure 9 shows the diameter of a closing pore as a function of time. The initial diameter was about 21 nm and it closes down completely in about 1 h. In this experiment, the rate of closing was roughly constant at a rate of 0.3 nm/min, at constant electron-beam intensity. This experiment clearly demonstrates that the rate of closing is slow enough to stop at any desired diameter, with single-nanometer resolution.

The rate of closing depends on the intensity of the beam; the higher the dose the higher the closing rate. We found that

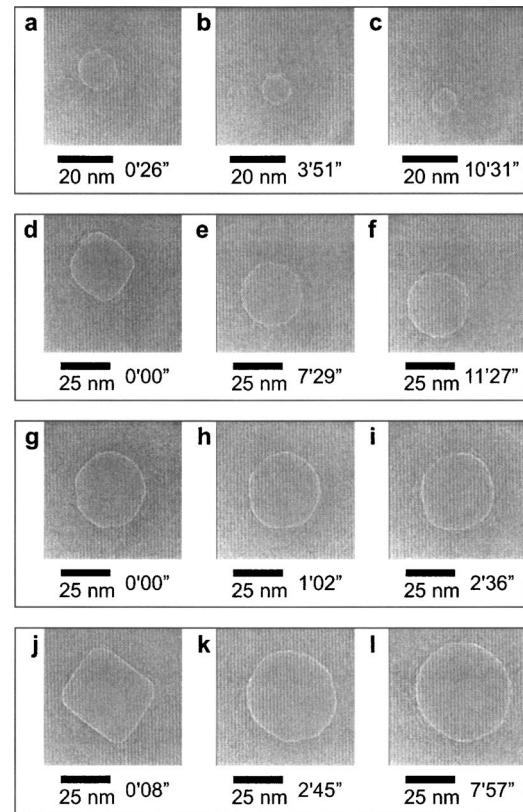


FIG. 8. Nanopore size and shape as a function of irradiation time (denoted at the bottom right below each image). (a)–(c) TEM micrographs of a nanopore with an initial size of about 15 nm. (d)–(f) TEM micrographs of a nanopore with an initial size of about 30 nm. (g)–(i) TEM micrographs of a nanopore with an initial size of about 35 nm. (j)–(l) TEM micrographs of a nanopore with an initial size of about 40 nm.

the closing rate for nanopores is not very reproducible from pore to pore, which prevented a systematic study. Even for pores in the same membrane with the same initial size and shape showed significantly different closing rates. Moreover, we found that some pores close at a constant rate, as shown in Fig. 9, while others shrink at increasing or decreasing rate.

E. Deforming a narrow slit

The effect of the electron beam on straight edges is demonstrated by imaging a 40-nm-wide slit with a spot size of

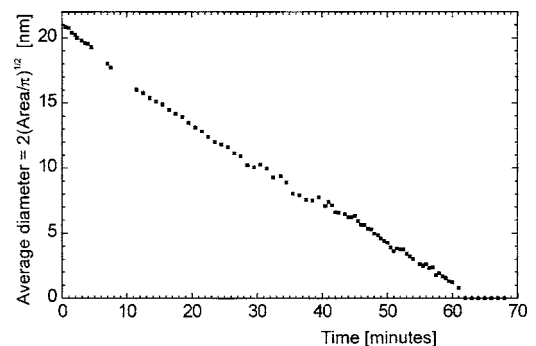


FIG. 9. Diameter vs time for a shrinking pore with an initial size of about 21 nm. A sequence of TEM micrographs was obtained using a charge-coupled device (CCD) camera during continuous electron irradiation at constant intensity and focus setting. From each image we determined the area of the pore, which was used to calculate the diameter, assuming a circular shape. The absolute error in this measurement is estimated to be 1 nm.

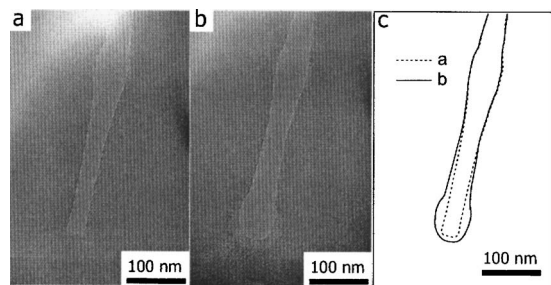


FIG. 10. (a) TEM micrograph of a slit in silicon oxide after TEM irradiation with an electron beam of about 150 nm near the top of the image. The slit has expanded only at the location of irradiation. (b) The same slit after irradiation at the end of the slit with an electron beam of about 150 nm. Again, the slit expands by the electron irradiation. (c) The edges of the slit in panels (a) and (b) are shown in one figure for comparison. Here we used the feature from the top of panel (a) for alignment.

about 150 nm. Figure 10(a) shows the resulting structure at a much lower magnification with a much larger beam. The slit was initially rectangular. At the location of the electron beam (near the top of the image), the slit has expanded considerably. On the same structure, we then imaged the end of the same slit with a spot size of again 150 nm. As shown in Fig. 10(b), the slit has become wider and longer at the end. In Fig. 10(c), we show the edges of the slit in these two micrographs to demonstrate the difference.

This experiment shows that the changes induced in a 40-nm-wide slit are very different to those observed in a $40 \times 40\text{-nm}^2$ pore: Only pores show shrinking behavior, while slits always widen. This difference will be addressed in Sec. IV. This experiment also demonstrates that the deformations are very local. The top part of the slit, only 300 nm away from the end, remains unchanged during the deformation of its end.

F. Elemental analysis on deforming pores

In this section, we discuss the possible changes to the material, caused by the high-intensity electron beam. This is an important issue because well-known effects observed in electron microscopy such as the deposition of carbon-rich contamination could provide an alternative mechanism for pore closure. We note that the dynamics of shrinking nanopores are unlike those of contamination growth. Contamination growth is observed as the buildup of material on an edge of the structure. This is not observed at all even if a very small and less-intense beam is used. During pore shrinkage, however, small features on the perimeter of the pore (it is

never perfectly circular) are preserved for quite some time. It thus appears that in our experiments, the edge itself appears to move inward, in agreement with our model. Another issue is electron-beam-induced depletion of the material. Such an effect could explain the observation of expanding pores. To shed light on these issues we performed control experiments where we measure the composition of the material of our devices inside an electron microscope.

First, we discuss a set of EDX experiments. The material irradiated by the electron beam emits x rays, and from the spectrum we obtain information on the elements present in the material. The “detection volume” is limited by the probe size and the thickness of the specimen. We obtained EDX spectra during a pore closing experiment. Figure 11(a) shows the orientation of our specimen relative to the beam and the detector in this experiment. The sample was tilted 15° towards the EDX detector. In this experiment, we shrunk a 50-nm pore to about 25 nm in 45 min. We used an electron beam of about $1\text{-}\mu\text{m}$ diameter and a dose of about $7 \times 10^4 \text{ A/m}^2$. Figure 11(b) shows an electron micrograph of the pore at the beginning of the experiment, and Fig. 11(c) at the end. Note that the TEM micrographs show noncircular pores. This is due to the tilt angle of the specimen. Figure 11(d) shows the EDX spectra obtained, where spectrum 1 is obtained at the start and spectrum 2 after the experiment. Clearly visible are the oxygen peak around 0.5 keV and the silicon peak around 1.8 keV. We find that the silicon peak stays constant, but the height of the oxygen peak is reduced by about 8%. From this experiment we estimate that the rate of oxygen loss is about 10%/h. The effect of oxygen loss from silicon oxide during electron irradiation has been studied in more detail by Chen *et al.*¹⁶ They have shown that this effect can be used to form silicon structures in an amorphous SiO_2 membrane. We note that the intensity of the electron beam used in their experiments was about $1 \times 10^9 \text{ A/m}^2$ orders of magnitude higher than in our experiments.

In our TECNAI microscope we performed an EELS experiment. We first closed down a nanopore in this TEM. Subsequently we performed an EELS experiment in imaging mode to ensure that only electrons are collected from the material that has filled the pore. The effective probe volume has a diameter of only 4 nm, determined by the magnification and the size of the input of the electron spectrometer. Figure 12 shows the result of this experiment. Figure 12(a) shows very clear peaks caused by silicon between 108 and 160 eV. The peaks at 108 and 112 eV are the Si-L_{2,3} peaks, and the peak at 156 eV is the Si-L₁ peak. Note that the

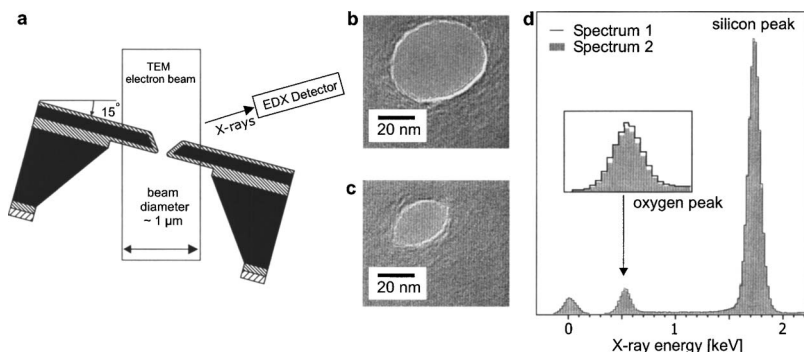


FIG. 11. (a) Orientation of nanopore device in electron microscope for EDX analysis. (b) Electron micrograph of the pore at the start of the EDX experiment. (c) The same pore at the end of the EDX experiment, 45 min later. (d) The EDX spectra obtained at the beginning (spectrum 1, black line) and at the end (spectrum 2, gray histogram) of the experiment. These data indicate a slow oxygen loss (10%/h).

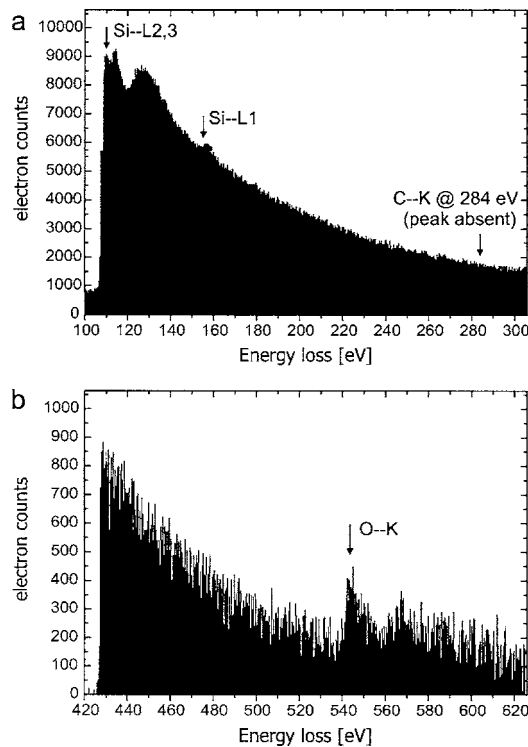


FIG. 12. Electron-energy-loss spectra obtained on the material that has filled a nanopore. (a) and (b) display the spectra at different energies. We clearly find the presence of silicon and oxygen around the center of the pore after shrinking. The absence of the C—K peak at 284 eV demonstrates that the carbon content of the material is below the detection limit of about 2 at. %.

positions of these peaks are different than those observed for pure silicon ($L_{2,3}$ at 101 eV, L_{1} at 150 eV). Importantly, we find no detectable carbon peak around 284 eV (C—K). We estimate that at most 2 at. % of the material consists of carbon. Figure 12(b) shows a peak around 545 eV (O—K), a clear sign of the presence of oxygen. These experiments prove that the material that closes our nanopores is predominantly silicon oxide.

IV. DISCUSSION

A. Electron-beam-induced modification of silicon oxide

It is well known that an electron beam of sufficient intensity can deform and damage materials. In electron microscopy, these effects are typically avoided but we have demonstrated that they can be used to obtain nanopores with well-defined dimensions. Typically, nanopores are closed using an electron dose between 10^4 and 10^7 A m⁻². At these irradiation levels, our nanopores deform while little chemical change could be detected. This strongly suggests that the amorphous silicon oxide is softened by the electron beam, and thus will deform as a viscous fluid. This claim is supported by the earlier work of Ajayan and Iijima,¹⁷ who observed electron-beam-induced flow of silicon oxide in sharp tips and wires at a similar electron dose.

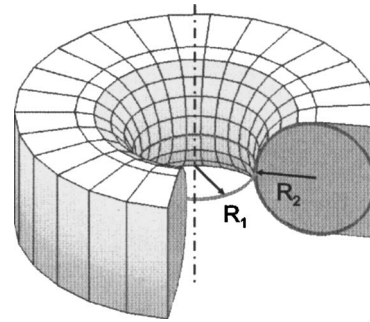


FIG. 13. Approximation of our nanopore geometry. The two radii of curvature of the siliconoxide surface are shown for the points that are closest to the axis of the pore. Note that R_1 is equal to the radius of the pore.

B. Modeling surface-tension-driven deformations

The magnitude of forces generated by surface tension depends strongly on the geometry of a surface. To explain our principal observation that pores below a certain critical size shrink, while larger ones expand, we briefly reiterate a simple model proposed in Ref. 7. We model our structure as a cylindrical hole with radius r in a film with uniform thickness h . We then calculate the difference in free energy of the perforated film with respect to the intact film. The free energy change ΔF is proportional to the change in surface area ΔA : $\Delta F = \gamma \Delta A = 2\pi\gamma(rh - r^2)$. The result is that, according to this model, pores with $2r < h$ can lower their free energy by shrinking and larger pores can do so by expanding. This effect qualitatively explains our experimental observations on deforming nanopores. The critical radius for this model is $r = h/2$. Taylor and Michael¹⁸ studied similar effects on holes in films of mercury on the millimeter scale, using optical microscopy. Lanxner *et al.*¹⁹ studied the effect of thermal annealing on nanometer-sized holes in 20-nm-thick crystalline gold films. Based on a comparison of hole sizes before and after annealing, he concluded that surface-tension-driven mass flow causes small pores to close down and large pores to expand.

While this model allows us to understand the simple physics behind the observed critical size, it has a number of limitations. A first point is that the pore is described by a single parameter r . A perfect cylindrical shape during shrinking is thus assumed. A second issue is that the total volume of the film is not constant in this model.

These limitations can be overcome by considering local forces generated by the surface tension. Laplace calculated that a curved surface under tension leads to a pressure difference over the interface. For a sphere this pressure difference is $\Delta P = 2\gamma/R$, where γ is the surface tension and R the radius of the sphere. On an arbitrary curved surface the pressure can be calculated with the Laplace–Young equation: $\Delta P = \gamma(1/R_1 + 1/R_2)$. Here R_1 and R_2 are the two local radii of curvature taken at perpendicular directions along the surface. Note that the sign of the radii should be taken into account; the net pressure at a “saddle” point with two opposite but equal curvatures will be zero. Figure 13 depicts a second model for our nanopores. Planar surfaces located near the pore have zero interface pressure difference. The pressure difference between points at the strongly curved surface in-

side the pore and points further away will lead to mass transport towards or away from the pore. We consider the circle of points at the surface closest to the axis. Figure 13 defines R_1 and R_2 , the two local radii of curvature. It follows immediately that for $R_1 < R_2$ there will be a Laplace pressure directed towards the axis of the pore, and as a consequence the pore will shrink. For $R_1 > R_2$, the net Laplace pressure is directed away from the axis, leading to expanding pores. In this approximation, R_2 is $h/2$ and we thus find a critical radius of $h/2$, in agreement with the simple free-energy argument.

Within this model the critical radius R_{critical} thus equals the radius of curvature of the aperture in the vertical direction R_2 . In the experiments described in Sec. III C we have indeed observed different critical radii for various values of R_2 . The curvature was approximated using the thickness of the oxide, as discussed in Sec. III A. We found critical diameters of 25 ± 10 nm and 80 ± 20 nm for oxide thicknesses of 20 and 50 nm, respectively. These values are in good agreement with the model, considering the approximations made.

The rounding of square apertures as shown in Fig. 6 can now also be understood: The curvatures are strongest in the corners of the square, and this will lead to the highest Laplace pressures towards the axis of the pore. These large forces lead to quick changes at the corners, as indeed observed in the experiment.

Furthermore, we can now explain the widening of a slit in silicon oxide during irradiation, as shown in Fig. 10(a). When we consider a point along the slit, away from the ends, we find that R_1 is effectively infinite, and thus there is no inward pressure. R_2 , however, is finite, and leads to a Laplace pressure that widens the slit. The effect at the end is more subtle: In addition to the widening effect for the long edges of the slit as discussed above, there is an inward pressure due to the corners of the slit where R_1 is small. In the experiment shown in Figs. 10(b) and 10(c) we see that the slit also expands at the end. Apparently the widening effect dominates, and shrinkage is only observed for pores smaller than the critical size.

V. CONCLUSION

We have discussed a new technique to fine tune the size of nanostructures with nanometer precision. These structures were fabricated in free standing silicon membranes with state-of-the-art silicon processes. Subsequently, we grow a thin layer of silicon oxide on the device by thermal oxidation. Our experiments demonstrate that this silicon oxide layer can be deformed locally with an electron beam of sufficient intensity, generated inside a transmission electron microscope. The process is particularly useful for the fabrication of nanopores: pores of 20–50-nm size can be shrunk to any desired dimension, with nanometer precision and with direct visual feedback.

We report a set of experiments that improve our understanding of the physical mechanism driving the nanostructure deformations upon electron-beam irradiation. We demonstrate that some pores shrink and others expand, based on their initial size. We conclude that the additional experiments and considerations further strengthen our hypothesis: An electron beam of sufficient intensity fluidizes the silicon oxide, and as a consequence the material will deform, driven by the surface tension of the material. We found no significant change in the composition of the nanostructures, and thus rule out contamination growth as a mechanism for pore closure.

ACKNOWLEDGMENTS

We thank Emile van der Drift, Bert Goudena, Arnold van Run, and Marc Zuiddam for assistance in clean-room processing and useful discussions. Ralph Smeets and Diego Krapf kindly supplied Fig. 5(e). This research was financially supported by the Dutch Foundation for Fundamental Research on Matter (FOM) and the Dutch Organisation for Scientific Research (NWO). One of the authors (J.H.C.) is grateful to the Netherlands Institute for Metals Research (NIMR) for financial support under Project No. MC4.98047. Another author (X.S.L.) acknowledges the support of the Guggenheim Foundation.

- ¹T. Ito and S. Okazaki, *Nature (London)* **406**, 1027 (2000).
- ²D. M. Eigler and E. K. Schweizer, *Nature (London)* **344**, 524 (1990).
- ³A. J. Heinrich, C. P. Lutz, J. A. Gupta, and D. M. Eigler, *Science* **298**, 1381 (2002).
- ⁴H. W. C. Postma, T. Teepen, Z. Yao, M. Grifoni, and C. Dekker, *Science* **293**, 76 (2001).
- ⁵A. F. Morpurgo, C. M. Marcus, and R. B. Robinson, *Appl. Phys. Lett.* **74**, 2064 (1999).
- ⁶J. L. Li, D. Stein, C. McMullan, D. Branton, M. J. Aziz, and J. A. Golovchenko, *Nature (London)* **412**, 166 (2001).
- ⁷A. J. Storm, J. H. Chen, X. S. Ling, H. W. Zandbergen, and C. Dekker, *Nat. Mater.* **2**, 537 (2003).
- ⁸J. L. Li, M. Gershow, D. Stein, E. Brandin, and J. A. Golovchenko, *Nat. Mater.* **2**, 611 (2003).
- ⁹A. J. Storm, C. Storm, J. H. Chen, H. W. Zandbergen, J. F. Joanny, and C. Dekker, *Nano Letters* (submitted).
- ¹⁰A. J. Storm, J. H. Chen, H. W. Zandbergen, and C. Dekker, *Phys. Rev. E* **71**, 051903 (2005).
- ¹¹A. Mara, Z. Siwy, C. Trautmanu, J. Wan, and F. Kamme, *Nano Lett.* **4**, 497 (2004).
- ¹²A. Aksimentiev, J. B. Heng, G. Timp, and K. Schulten, *Biophys. J.* **87**, 2086 (2004).
- ¹³H. Chang, F. Kosari, G. Andreadakis, M. A. Alam, G. Vasmatzis, and R. Bashir, *Nano Lett.* **4**, 1551 (2004).
- ¹⁴N. N. Gribov, S. J. C. H. Theeuwen, J. Caro, and S. Radelaar, *Microelectron. Eng.* **35**, 317 (1997).
- ¹⁵*Handbook of Microlithography, Micromachining and Microfabrication*, edited by P. Rai-Choudhury (SPIE, Bellingham, WA, 1997).
- ¹⁶G. S. Chen, C. B. Boothroyd, and C. J. Humphreys, *Appl. Phys. Lett.* **62**, 1949 (1993).
- ¹⁷P. M. Ajayan and S. Iijima, *Philos. Mag. Lett.* **65**, 43 (1992).
- ¹⁸G. I. Taylor and D. H. Michael, *J. Fluid Mech.* **58**, 625 (1973).
- ¹⁹M. Lanxner, C. L. Bauer, and R. Scholz, *Thin Solid Films* **150**, 323 (1987).